

# Strain engineering and epitaxial stabilization of halide perovskites

<https://doi.org/10.1038/s41586-019-1868-x>

Received: 12 April 2019

Accepted: 19 November 2019

Published online: 8 January 2020

Yimu Chen<sup>1,8</sup>, Yusheng Lei<sup>1,8</sup>, Yuheng Li<sup>1</sup>, Yugang Yu<sup>2</sup>, Jinze Cai<sup>2</sup>, Ming-Hui Chiu<sup>3</sup>, Rahul Rao<sup>4</sup>, Yue Gu<sup>2</sup>, Chunfeng Wang<sup>1</sup>, Woojin Choi<sup>5</sup>, Hongjie Hu<sup>2</sup>, Chonghe Wang<sup>1</sup>, Yang Li<sup>1</sup>, Jiawei Song<sup>2</sup>, Jingxin Zhang<sup>2</sup>, Baiyan Qi<sup>2</sup>, Muyang Lin<sup>1</sup>, Zhuorui Zhang<sup>1</sup>, Ahmad E. Islam<sup>4</sup>, Benji Maruyama<sup>4</sup>, Shadi Dayeh<sup>1,2,5</sup>, Lain-Jong Li<sup>3,6</sup>, Kesong Yang<sup>1</sup>, Yu-Hwa Lo<sup>2,5</sup> & Sheng Xu<sup>1,2,5,7\*</sup>

Strain engineering is a powerful tool with which to enhance semiconductor device performance<sup>1,2</sup>. Halide perovskites have shown great promise in device applications owing to their remarkable electronic and optoelectronic properties<sup>3–5</sup>. Although applying strain to halide perovskites has been frequently attempted, including using hydrostatic pressurization<sup>6–8</sup>, electrostriction<sup>9</sup>, annealing<sup>10–12</sup>, van der Waals force<sup>13</sup>, thermal expansion mismatch<sup>14</sup>, and heat-induced substrate phase transition<sup>15</sup>, the controllable and device-compatible strain engineering of halide perovskites by chemical epitaxy remains a challenge, owing to the absence of suitable lattice-mismatched epitaxial substrates. Here we report the strained epitaxial growth of halide perovskite single-crystal thin films on lattice-mismatched halide perovskite substrates. We investigated strain engineering of  $\alpha$ -formamidinium lead iodide ( $\alpha$ -FAPbI<sub>3</sub>) using both experimental techniques and theoretical calculations. By tailoring the substrate composition—and therefore its lattice parameter—a compressive strain as high as 2.4 per cent is applied to the epitaxial  $\alpha$ -FAPbI<sub>3</sub> thin film. We demonstrate that this strain effectively changes the crystal structure, reduces the bandgap and increases the hole mobility of  $\alpha$ -FAPbI<sub>3</sub>. Strained epitaxy is also shown to have a substantial stabilization effect on the  $\alpha$ -FAPbI<sub>3</sub> phase owing to the synergistic effects of epitaxial stabilization and strain neutralization. As an example, strain engineering is applied to enhance the performance of an  $\alpha$ -FAPbI<sub>3</sub>-based photodetector.

$\alpha$ -FAPbI<sub>3</sub> is epitaxially grown on a series of mixed methylammonium lead chloride/bromide (MAPbCl<sub>x</sub>Br<sub>3-x</sub>) single crystalline substrates by the inverse temperature growth method<sup>16</sup>. The resulting MAPbCl<sub>x</sub>Br<sub>3-x</sub> substrates, with different compositional ratios and thus lattice parameters, are grown by solutions with different Cl/Br precursor molar ratios (Supplementary Fig. 1)<sup>17</sup>. We note that the strain in the epilayer is determined not only by the lattice mismatch, but also by the relaxation mechanisms. Lattice distortion relaxes the strain, so the region near the heteroepitaxy interface has the highest strain, which gradually drops at regions distant from the interface. The total elastic strain energy increases as the film grows thicker, until it eventually crosses the threshold energy for structural defect generation, and dislocations will form to partially relieve the misfit<sup>18</sup>. A slow growth rate of the epilayer is chosen, as a higher rate will increase the defect concentration in the epilayer. The crystalline quality of the substrates is carefully optimized, as the defects in the substrates can propagate into the epilayer (Extended Data Fig. 1).

Heteroepitaxial growth leads to controllable film thickness, preferential growth sites and orientations, compatible fabrication protocols

with existing infrastructures and scalable large-area device applications. Figure 1a shows optical images of a series of MAPbCl<sub>x</sub>Br<sub>3-x</sub> substrates with a layer of epitaxial  $\alpha$ -FAPbI<sub>3</sub> film on the top. The epilayer has a uniform thickness with a well defined film–substrate interface (Fig. 1b). The film topography can reveal the growth mechanism and sometimes the defects caused by strain relaxation. On the one hand, a sub-100 nm  $\alpha$ -FAPbI<sub>3</sub> thin film shows a clear interface (Fig. 1b), and a well defined terrain morphology, with a step height close to the size of a  $\alpha$ -FAPbI<sub>3</sub> unit cell, indicating layer-by-layer growth behaviour of the epitaxial  $\alpha$ -FAPbI<sub>3</sub> (Extended Data Fig. 2a, b). A 10-μm film, on the other hand, shows non-conformal growth, indicating strain relaxation by dislocation formation (Extended Data Fig. 2c, d).

The crystallographic relationships between the MAPbCl<sub>x</sub>Br<sub>3-x</sub> substrates and the epitaxial  $\alpha$ -FAPbI<sub>3</sub> thin films are illustrated by high-resolution X-ray diffraction (XRD) (Fig. 1c). In their freestanding form, both  $\alpha$ -FAPbI<sub>3</sub> and MAPbCl<sub>x</sub>Br<sub>3-x</sub> have a cubic structure<sup>19,20</sup>. The lattice parameters of freestanding  $\alpha$ -FAPbI<sub>3</sub> and MAPbCl<sub>x</sub>Br<sub>3-x</sub> substrates (both with  $Pm\bar{3}m$  space group) are calculated to be 6.35 Å (Supplementary Fig. 1) and 5.83–5.95 Å, respectively. The ratio  $x$  for each

<sup>1</sup>Department of Nanoengineering, University of California San Diego, La Jolla, CA, USA. <sup>2</sup>Materials Science and Engineering Program, University of California San Diego, La Jolla, CA, USA.

<sup>3</sup>Physical Science and Engineering Division, King Abdullah University of Science and Technology, Thuwal, Saudi Arabia. <sup>4</sup>Materials and Manufacturing Directorate, Air Force Research

Laboratory, Wright Patterson Air Force Base, Dayton, OH, USA. <sup>5</sup>Department of Electrical and Computer Engineering, University of California San Diego, La Jolla, CA, USA. <sup>6</sup>School of Materials Science and Engineering, University of New South Wales, Sydney, New South Wales, Australia. <sup>7</sup>Department of Bioengineering, University of California San Diego, La Jolla, CA, USA. <sup>8</sup>These authors contributed equally: Yimu Chen, Yusheng Lei. \*e-mail: shengxu@ucsd.edu

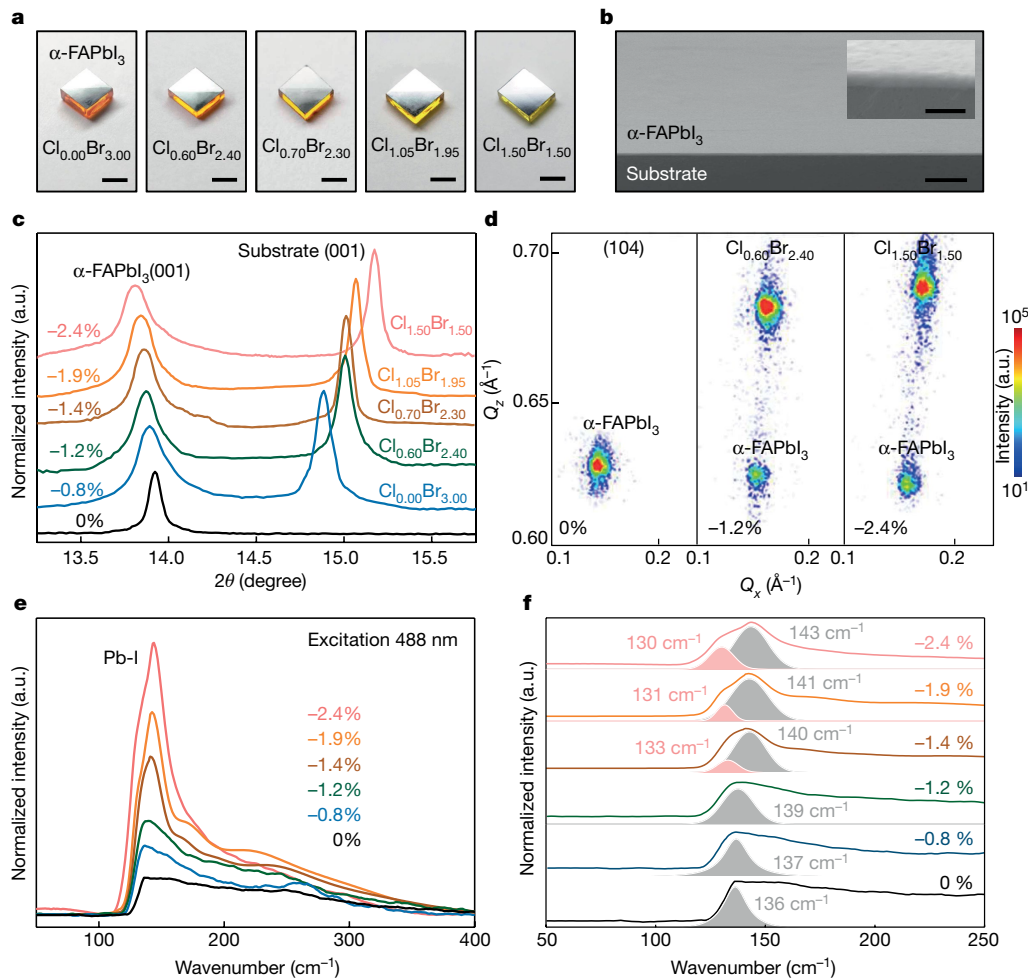


**Fig. 1 | Epitaxial  $\alpha$ -FAPbI<sub>3</sub> thin films and structural characterizations.** **a**, Optical images of the as-grown epitaxial  $\alpha$ -FAPbI<sub>3</sub> thin films. The high transparency of the substrates and the smooth surfaces of the thin films demonstrate their high quality. Scale bars, 4 mm. **b**, A cross-sectional scanning electron microscope (SEM) image of the epitaxial thin film with controlled uniform thickness. Scale bar, 2  $\mu$ m. Inset, magnified SEM image of the heterostructure showing a well defined interface. Scale bar, 200 nm. **c**, High-resolution XRD  $\omega - 2\theta$  scan of the (001) peaks of the epitaxial samples on different substrates showing the increasing tetragonality with increasing lattice mismatch. **d**, Reciprocal space mapping with (104) asymmetric reflection of the  $\alpha$ -FAPbI<sub>3</sub> for different lattice mismatches with the substrate. The results show a decrease in the in-plane lattice parameter as well as an

increase in the out-of-plane lattice parameter with larger compressive strain.  $Q_x$  and  $Q_z$  are the in-plane and out-of-plane reciprocal space coordinates.

**e**, Confocal Raman spectra of the epitaxial layer at different strains. We attribute the evolution of the shape and intensity of the peak with strain to the increase in lattice tetragonality under higher strain. We note that the broad peak at approximately 250 cm<sup>-1</sup> is attributed to the Pb-O bond induced by laser oxidation. **f**, Fitting analysis of the Raman peaks. The peak at 136 cm<sup>-1</sup> from the strain-free sample (black line) is attributed to the Pb-I bond. With increasing compressive strain, the peak gradually blueshifts as the bond becomes more rigid, and finally splits into a main peak that blueshifts (owing to in-plane bond contraction) and a shoulder peak that redshifts (owing to out-of-plane bond extension). (a.u., arbitrary units).

composition is then calculated to be 0–1.50, according to the Vegard's Law (Supplementary Table 1). As  $x$  increases, the MAPbCl<sub>x</sub>Br<sub>3-x</sub> (001) peaks shift to a higher  $2\theta$  angle, indicating a decrease in the lattice parameters of the substrate and therefore an increase in the lattice mismatch (Fig. 1c and Supplementary Table 2). Meanwhile, the  $\alpha$ -FAPbI<sub>3</sub> (001) peak shifts to a lower  $2\theta$  angle, indicating an increase in the out-of-plane lattice parameter as the in-plane compressive strain increases. When  $x$  exceeds 1.50, the strain energy dramatically increases, and the epitaxial growth becomes less thermodynamically favourable.  $\alpha$ -FAPbI<sub>3</sub> then randomly crystallizes on the substrate (Supplementary Fig. 2). Peak broadening of the epitaxial  $\alpha$ -FAPbI<sub>3</sub> is therefore induced by the epitaxial strain and the reduction in film thickness, instead of by the strain-induced dislocations or the strain relaxation (Supplementary Fig. 3). Figure 1d shows the reciprocal space mapping of strain-free and strained  $\alpha$ -FAPbI<sub>3</sub> thin films with different lattice mismatch with the substrate. An increase of tetragonality of the lattice is evident as the compressive strain increases.

The corresponding strain levels of the  $\alpha$ -FAPbI<sub>3</sub> in those three cases are calculated to be 0%, -1.2% and -2.4%, respectively, on the basis of the lattice distortion (where the negative sign denotes compressive strain). The Poisson's ratio is determined to be around 0.3, which is consistent with the reported value<sup>21</sup>.

We also studied the structure of  $\alpha$ -FAPbI<sub>3</sub> at different strains (between 0% and -2.4%, on different substrates) by Raman spectroscopy (Fig. 1e). Control experiments exclude any Raman signals from the substrates (Supplementary Fig. 4). The peak at around 136 cm<sup>-1</sup> in Fig. 1e, which originated from the stretching of the lead-iodine bond<sup>22</sup>, increases in intensity and broadens in width as the strain increases. The cubic structure of the strain-free  $\alpha$ -FAPbI<sub>3</sub> is less Raman-active, and the detectable signal is usually broad and weak. When in-plane compressive strain increases, the inorganic framework gradually gains tetragonality and produces a stronger Raman signal with a clearly distinguishable shape. Interestingly, at around -1.4% strain, the peak at 136 cm<sup>-1</sup> starts to split into two: a main peak at about 140 cm<sup>-1</sup> and a

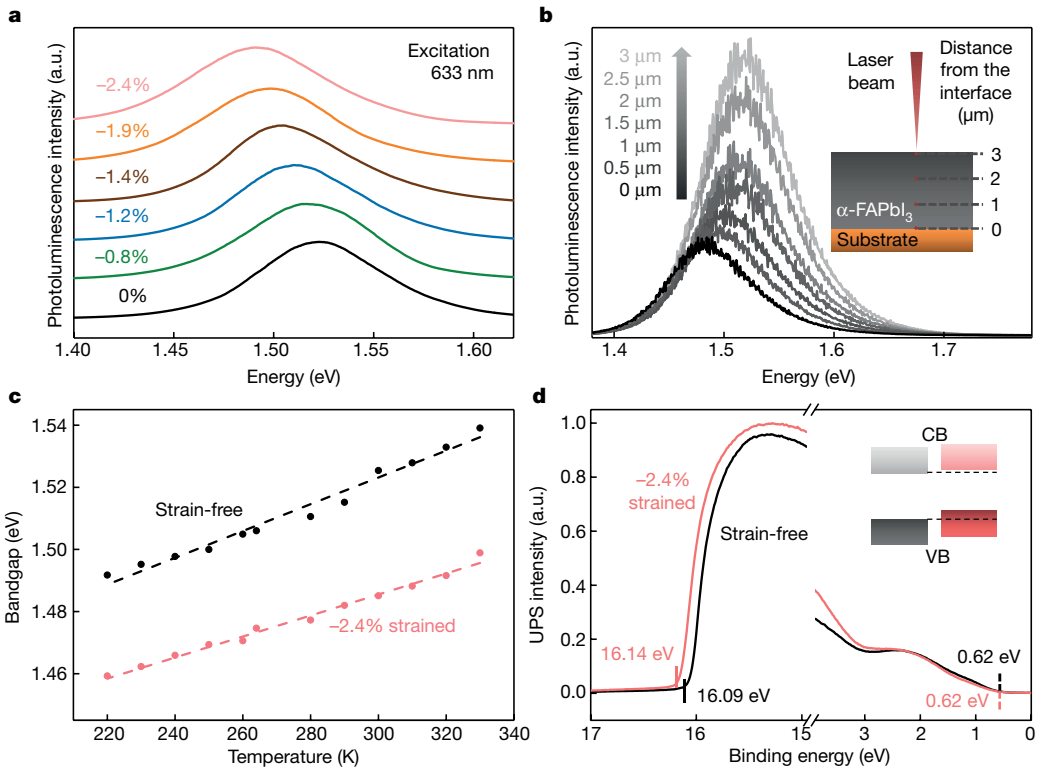


**Fig. 2 | Optical properties.** **a**, Photoluminescence spectra of  $\alpha$ -FAPbI<sub>3</sub> at different strains. The redshift of the photoluminescence peak with increasing strain is due to bandgap reduction under compressive strain, consistent with the first-principles calculations. **b**, Focal-point-dependent confocal photoluminescence spectra of a 3- $\mu\text{m}$ -thick film. When the focal point of the laser (indicated by the red point in the schematic; inset) moves towards the epitaxial interface, the photoluminescence emission peak shifts from about 1.523 eV to about 1.479 eV, owing to the large compressive strain close to the interface. **c**, Temperature-dependent photoluminescence spectra of a -2.4% strained and a strain-free sample. The bandgap of the strain-free sample shows

a stronger temperature dependence than the strained sample, indicating that the substrate can reduce the lattice deformation that is caused by the temperature change. **d**, UPS spectra of a -2.4% strained and a strain-free sample. The Fermi level and the VBM of the samples can be extracted from the intersections of the curves with the horizontal axis, marked by the solid and dashed vertical lines, respectively. The results reveal that compressive strain increases the VBM more than it does the CBM, owing to the enhanced interaction of lead 6s and iodine 5p orbitals under the compressive strain. Inset, the schematic band diagram of the -2.4% strained and strain-free samples. CB, conduction band; VB, valence band.

shoulder at about 133 cm<sup>-1</sup> (Fig. 1f). When the strain is further increased to -2.4%, these two peaks shift to 143 cm<sup>-1</sup> and 130 cm<sup>-1</sup>, respectively. We attribute the blueshift of the main peak to the compression of the in-plane lead–iodine bond, and the redshift of the shoulder peak to the stretching of the out-of-plane lead–iodine bond. This result is also supported by the simulated Raman spectra by first-principles calculations (Supplementary Fig. 4c, d). We also studied the Raman spectra of  $\alpha$ -FAPbI<sub>3</sub> of various thicknesses on MAPbCl<sub>1.50</sub>Br<sub>1.50</sub> (Supplementary Fig. 4f). The results are consistent: a strong, sharp peak is detected from a sub-100-nm film with -2.4% strain, and a weak, broad peak is detected from a film of around 2  $\mu\text{m}$ , where the misfit strain is relaxed near the film surface.

Photoluminescence spectra (Fig. 2a) reveal changes in the bandgap of sub-100-nm epitaxial  $\alpha$ -FAPbI<sub>3</sub> thin films under different strains (between 0% and -2.4%, on different substrates). The photoluminescence peak of  $\alpha$ -FAPbI<sub>3</sub> gradually shifts from about 1.523 eV at 0% strain to about 1.488 eV at -2.4% strain, corresponding to a reduction of about 35 meV in the bandgap. We exclude the possible contributions to this photoluminescence redshift from thickness-dependent bandgap<sup>23,24</sup>, reabsorption<sup>25</sup> or halide migration<sup>26</sup> (detailed discussions in the Supplementary Information). The bandgap change is consistent with the first-principles calculations and absorption measurements (Extended Data Fig. 3). The photoluminescence peak in Fig. 2a also broadens with increasing strain (Supplementary Fig. 5), which is not due to possible charge transfer between the epitaxial  $\alpha$ -FAPbI<sub>3</sub> and the substrate (Supplementary Fig. 6).

Temperature-dependent photoluminescence studies suggest that the emission peak broadening originates from the reduced crystalline quality and the enhanced carrier–phonon coupling under the strain (Extended Data Fig. 4).

Additionally, we studied confocal photoluminescence spectra at different locations in an  $\alpha$ -FAPbI<sub>3</sub> film of around 3  $\mu\text{m}$  on a substrate of MAPbCl<sub>1.50</sub>Br<sub>1.50</sub> (Fig. 2b). The photoluminescence peak shifts from about 1.479 eV when the laser is focused at the interface where the local strain is high, to about 1.523 eV at 3  $\mu\text{m}$  from the interface where the strain is relaxed. As a control, the photoluminescence redshift in a strain-free sample is less obvious (from about 1.516 eV to about 1.523 eV, Supplementary Fig. 7a), which is attributed to reabsorption<sup>25</sup>. In the strained sample, we exclude elastic relaxation although halide perovskites are much softer than conventional semiconductors<sup>27</sup>. Our finite element analysis simulation results show that the elastic relaxation for a 3- $\mu\text{m}$ -thick  $\alpha$ -FAPbI<sub>3</sub> thin film is negligible: only around 0.09% (Supplementary Fig. 8). Thickness-dependent in-plane XRD is used to study the critical thickness at which the strain will start to be plastically relaxed (Extended Data Fig. 5). The results show that the critical thickness is much less than the thickness we used in this study and, therefore, the relaxation can be attributed to plastic relaxation by the formation of dislocations. Photoluminescence measurements from samples of different thicknesses show a similar trend (Supplementary Fig. 9), indicating that the strain is relaxed by dislocations when the film grows thicker. Temperature-dependent photoluminescence studies indicate that the bandgap of  $\alpha$ -FAPbI<sub>3</sub>

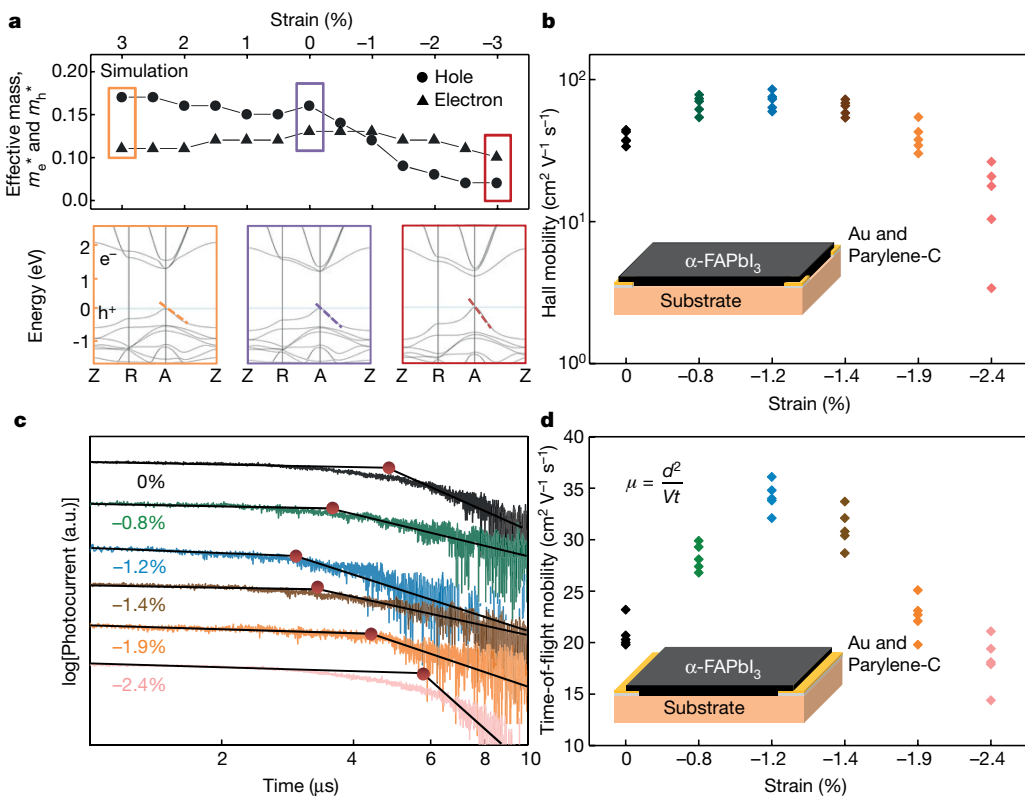


**Fig. 3 | Electronic properties.** **a**, Calculated effective masses of the carriers at different strains, and electronic bandstructures under three strain levels (3%, 0% and -3%). The electron effective mass ( $m_e^*$ ) remains relatively stable with the change in strain, while the hole effective mass ( $m_h^*$ ) decreases with increasing compressive strain. The dashed lines represent the dispersivity of the valence band; a less dispersive valence bandstructure indicates a smaller hole effective mass. The Z, R and A points are high-symmetry points in the first Brillouin zone of the tetragonal lattice. Bottom panels with coloured borders represent three typical examples with different strains. **b**, Hole mobilities by Hall effect measurements showing that  $\alpha\text{-FAPbI}_3$  with strain of -1.2% has the highest hole mobility. Coloured symbols correspond to the strain as in **c**. The decrease of the hole mobility with strain higher than -1.2% is attributed to the increase of dislocation density. Number of experiments,  $n=5$  for each strain. Inset, the

structure of the measurement setup (gold, yellow; parylene-C, grey), not to scale. **c**, Transient photocurrent curves of the epitaxial  $\alpha\text{-FAPbI}_3$  under different strains. The transient photocurrent curves are plotted on a log-log scale. The carrier transit time—that is, the inflection point of the photocurrent curve—is marked by a solid red circle. The inflection point indicates the point at which the charge transport carriers switch from the majority to the minority carriers. Lines are guides to the eye. **d**, Plots of calculated carrier mobilities as a function of the strain magnitudes. The inset equation,  $\mu = d^2/Vt$ , transforms the carrier transit time to the carrier mobility, where  $\mu$  is the calculated time-of-flight carrier mobility,  $d$  is the target region thickness,  $V$  is the applied voltage and  $t$  is the measured carrier transit time. Number of experiments,  $n=5$  for each strain. Inset, schematic measurement setup. Coloured symbols correspond to the strain as in **c**.

under both 0% and -2.4% strain shows a strong temperature dependence, owing to the soft nature of  $\alpha\text{-FAPbI}_3$  (Fig. 2c and Extended Data Fig. 4)<sup>7</sup>. The strained-sample bandgap is less temperature-dependent compared to that of the strain-free sample, because the smaller thermal expansion coefficient of the substrate compared to the epitaxial layer introduces a constraint<sup>28</sup> (detailed discussions in the Supplementary Information).

Ultraviolet photoelectron spectroscopy (UPS) reveals the band-structure evolution of the  $\alpha\text{-FAPbI}_3$  under strain (see Fig. 2d for 0% and -2.4% strain and Extended Data Fig. 6 for other strains). All samples exhibit p-type behaviour (see Supplementary Information for more details). The Fermi level and the valence-band maximum (VBM) of the samples can be extracted from the UPS data. The results show that strain of -2.4% lifts the VBM upward by about 50 meV compared to the strain-free scenario. Considering the change in the bandgap (about 35 meV, Fig. 2a), the -2.4% strain pushes the conduction-band minimum (CBM) upward by about 15 meV compared to the strain-free scenario. The VBM mainly consists of lead 6s and iodine 5p orbitals, and the enhanced coupling between these orbitals under compressive strain pushes the VBM upward<sup>29</sup>. The CBM, which consists mostly of nonbonding localized states of Pb p orbitals, is less sensitive to the deformation of the  $\text{PbI}_6$  octahedrons<sup>7</sup>. Therefore, the in-plane compressive strain increases the VBM more than it does the CBM.

The lattice deformation can alter the electronic bandstructure and therefore also the carrier dynamics. The effective mass of charge carriers can be assessed by the band curvature extracted from first-principles calculations<sup>30</sup>. Figure 3a shows the calculated results of the electron effective mass,  $m_e^*$ , and hole effective mass,  $m_h^*$  (the top panel) and three typical electronic bandstructures (the bottom panels) under different strains. On the one hand, the E-k dispersion of the conduction band remains relatively unaltered, and  $m_e^*$  shows only a slight variation under strain between 3% and -3%. On the other hand, compressive strain can modulate the E-k dispersion of the valence band and considerably reduce  $m_h^*$ .

To validate these calculations, Hall effect carrier mobilities of the  $\alpha\text{-FAPbI}_3$  thin films under strain of between 0% and -2.4% are measured (Fig. 3b). Finite element analysis simulation results show that potential carrier transfer from the substrate to the epitaxial layer is negligible, owing to an insulating layer (Parylene-C) and the energy barrier between the epitaxial layer and the substrate (Supplementary Fig. 10). All samples measured by the Hall effect show a p-type character, which is consistent with the UPS results. Of all strain levels tested, films under -1.2% strain on a  $\text{MAPbCl}_{0.60}\text{Br}_{2.40}$  substrate have the highest hole mobility (Fig. 3b). Further increasing the strain results in a drastic drop in the hole mobility, because of the higher dislocation densities that arise at higher strain levels. We note that the devices for

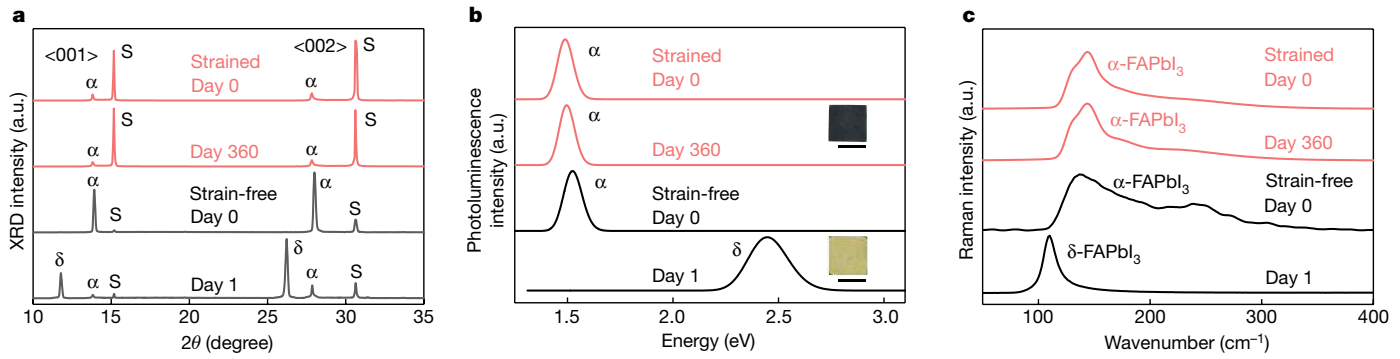


**Fig. 4 | Epitaxial stabilization.** **a**, Phase stability comparison of thin (sub-100 nm, ~2.4% strained; pink) and thick (about 10  $\mu\text{m}$ , strain-free; black) epitaxial  $\alpha$ -FAPbI<sub>3</sub> on MAPbCl<sub>1.50</sub>Br<sub>1.50</sub> substrates by XRD.  $\alpha$ ,  $\alpha$ -FAPbI<sub>3</sub>;  $\delta$ ,  $\delta$ -FAPbI<sub>3</sub>; S, substrate. The thin, strained sample shows better phase stability (red curves). For the thick, strain-free sample, the (001) peak for  $\alpha$ -FAPbI<sub>3</sub> at 13.9° is the same as the strain-free sample in Supplementary Fig. 1a, which indicates that the top surface of the thick sample is fully relaxed (day 0, black curve). The X-ray can penetrate about 10–20  $\mu\text{m}$  into the halide perovskites, which explains why the substrate peaks are more intense in the thin sample than in the thick sample. The thick, strain-free sample shows signs of a phase transition to  $\delta$ -FAPbI<sub>3</sub> after 24 h (lower black curve). **b**, Phase stability study by photoluminescence spectroscopy. Re-measurement of the thin, strained sample after 360 d (lower pink curve) shows no obvious photoluminescence peak shift, but does show a slight decrease in peak intensity owing to its natural

degradation into PbI<sub>2</sub> (ref. <sup>16</sup>). For the thick, strain-free sample, the photoluminescence spectrum shows an emission peak close to 1.52 eV, similar to that in the strain-free  $\alpha$ -FAPbI<sub>3</sub> bulk crystal shown in Fig. 2a, indicating a full strain relaxation in the thick sample. Re-measurement after 24 h (lower black curve) shows that the thick film undergoes a transition from the  $\alpha$  phase to the  $\delta$  phase. Insets, optical images of the two samples, showing clear visual clues of the phase stability in the thin, strained sample (black  $\alpha$  phase) and the phase transition in the thick, strain-free sample (yellow  $\delta$  phase) after 24 h. Scale bars, 2 mm. **c**, Phase stability study by Raman spectroscopy. The Raman characteristics of the thin, strained sample show a peak at 143  $\text{cm}^{-1}$  with no substantial difference after 360 d; the thick, strain-free sample (peak at 136  $\text{cm}^{-1}$ ) shows signs of a phase transformation to  $\delta$ -FAPbI<sub>3</sub> after 24 h, as revealed by its signature peak at 108  $\text{cm}^{-1}$ .

Hall effect measurements have an epitaxial-layer thickness larger than the critical thickness to ensure sufficient contact area between the halide perovskite and the bottom electrode. Therefore, a high strain level will induce a high concentration of dislocations that degrade the hole mobility.

To validate the Hall mobility, we carried out time-of-flight measurements. The transient photocurrents after single excitation are plotted logarithmically in Fig. 3c. The carrier transit time shows the smallest value of the film under ~1.2% strain. The calculated carrier mobility is plotted as a function of the strain applied (Fig. 3d, see the Supplementary Information for calculation details), and shows a similar trend to that given by the Hall effect. We note that the absolute mobility values from the time-of-flight and Hall effect measurements differ, owing to experimental uncertainties in the type and quality of electronic contacts made during the fabrication processes<sup>31</sup>. The space-charge-limited-current method can quantify trap density<sup>32</sup>. Results show that a higher strain level leads to a higher trap density (Extended Data Fig. 7 and Supplementary Fig. 11), which explains the observed decrease in mobility under a higher strain magnitude. Capacitance–frequency ( $C$ – $\omega$ ) spectroscopy is also used to cross-check the trap density (Supplementary Fig. 12), the results of which correspond well with those obtained by the space-charge-limited-current method.

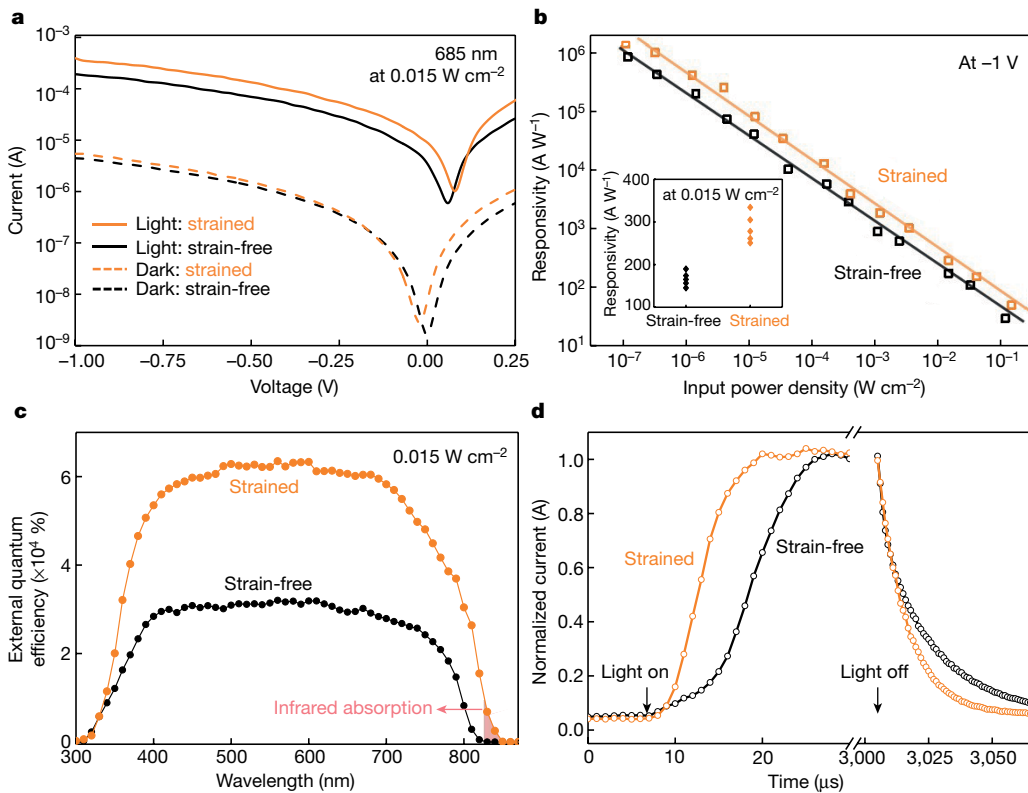
It is widely accepted that  $\alpha$ -FAPbI<sub>3</sub> crystals are metastable at room temperature and can quickly phase transform to photo-inactive  $\delta$ -FAPbI<sub>3</sub> within approximately 24 h (ref. <sup>16</sup>), owing to its internal lattice strain and low entropy<sup>19,33</sup>. Existing strategies for  $\alpha$ -FAPbI<sub>3</sub> stabilization, including alloying<sup>26</sup> and surface passivation<sup>34</sup>, either widen the bandgap or raise the carrier transport barrier by introducing nonconductive ligands (detailed discussions in the Supplementary Information). However, the epitaxial  $\alpha$ -FAPbI<sub>3</sub> thin film exhibits long-lasting phase stability at room temperature.

Figure 4a shows XRD results of a sub-100-nm epitaxial  $\alpha$ -FAPbI<sub>3</sub> thin film that is stable for at least 360 d after growth (red curves in Fig. 4a). In the 10- $\mu\text{m}$  epitaxial thick film (far beyond the threshold thickness at which the strain is fully relaxed), the stabilization effect disappears: after 24 h, XRD peaks from  $\delta$ -FAPbI<sub>3</sub> can be detected (black curves in

Fig. 4a). The phase stability of the strained  $\alpha$ -FAPbI<sub>3</sub> is also verified by photoluminescence (Fig. 4b) and Raman spectroscopy (Fig. 4c). A possible stabilization effect from incorporating bromine or chlorine into the  $\alpha$ -FAPbI<sub>3</sub> can be excluded, because those foreign ions would stabilize the  $\alpha$ -phase regardless of the epilayer thickness. X-ray photoelectron spectroscopy (XPS) measurements showing the absence of bromine and chlorine provide additional evidence that this is not the origin of the stability (Extended Data Fig. 8).

The mechanism of the stable thin  $\alpha$ -FAPbI<sub>3</sub> can be explained by two reasons. First, the interfacial energy of cubic  $\alpha$ -FAPbI<sub>3</sub>/cubic substrate is much lower than that of hexagonal  $\delta$ -FAPbI<sub>3</sub>/cubic substrate, which is the most critical factor for the stabilization effect (Supplementary Fig. 13, Supplementary Table 3, and see Supplementary Information for details). The epitaxial lattice is constrained to the substrate owing to the strong ionic bonds between them and, therefore, the lattice is restricted from the phase transition. Second, the driving force of the  $\alpha$ -to- $\delta$  phase transition is believed to be the internal tensile strain in the  $\alpha$ -FAPbI<sub>3</sub> unit cell, which can induce the formation of vacancies and subsequent phase transition<sup>35</sup>. In this study, the epitaxial film is under compressive strain, which neutralizes the effect of the internal tensile strain. Therefore, the synergistic effect of the low-energy coherent epitaxial interface and the neutralizing compressive strain are the key to  $\alpha$ -FAPbI<sub>3</sub> stabilization. As a control, epitaxial  $\alpha$ -FAPbI<sub>3</sub> thin film is removed from the substrate (Supplementary Fig. 14); the removed  $\alpha$ -FAPbI<sub>3</sub> transforms to the  $\delta$  phase within 24 h.

We demonstrate high-responsivity photodetectors as a use case of the strain engineered  $\alpha$ -FAPbI<sub>3</sub> thin film. Figure 5a shows the current–voltage ( $I$ – $V$ ) characteristics of a strain-free device and a device under ~1.2% strain. The dark current at -1 V in the strained device is around 15% higher than that in the strain-free one, indicating the higher defect density of the strained device. However, the photocurrent in the strained device increases by approximately 180% compared to the strain-free device. We attribute the photocurrent increase to higher carrier mobility and better alignment of VBM to the Fermi level of the gold electrode under compressive strain (Supplementary Fig. 15).



**Fig. 5 | Photodetector characterizations of the  $\alpha$ -FAPbI<sub>3</sub> thin films.** **a**,  $I$ - $V$  characteristics of Au/ $\alpha$ -FAPbI<sub>3</sub>/indium tin oxide photoconductor structured photodetectors. The dark current and photocurrent of the  $-1.2\%$  strained detector are about 15% and 180% higher than those of its strain-free counterpart. Detectors are tested with a 685-nm laser under  $0.015\text{ W cm}^{-2}$ . **b**, Comparison of responsivity of the  $-1.2\%$  strained and strain-free photodetectors. The responsivity of both devices shows an increasing trend with decreasing incident power, as the chances of carrier recombination go down at low illumination intensities<sup>36</sup>. The strained device yields a higher

responsivity owing to higher carrier mobility and better band alignment. Inset, the statistical average of the detector performance. Number of experiments,  $n=5$  for each strain value. **c**, External quantum efficiency spectra of the  $-1.2\%$  strained and strain-free photodetectors showing that the strained photodetector yields a higher external quantum efficiency as well as a broader absorption spectrum (Extended Data Fig. 9d), owing to enhanced carrier mobility and bandgap reduction. **d**, Response times of the photodetectors, with faster rise and fall times for the  $-1.2\%$  strained ( $9\text{ }\mu\text{s}$  and  $34\text{ }\mu\text{s}$ ) than the strain-free ( $14\text{ }\mu\text{s}$  and  $50\text{ }\mu\text{s}$ ) device due to the enhanced carrier mobility and transport.

Responsivity of the two photodetectors—defined as the change in photocurrent per unit of illumination intensity—is measured at various illumination intensities (Fig. 5b). The responsivity of the strained device, which reaches a maximum of  $1.3 \times 10^6\text{ A W}^{-1}$  at an incident power density of  $1.1 \times 10^{-7}\text{ W cm}^{-2}$ , is almost twice of that of the strain-free device. This is again attributed to the enhanced carrier mobility and the better band alignment of the strained device. The responsivity of this strained device is, to our knowledge, the highest reported for a  $\alpha$ -FAPbI<sub>3</sub> device under similar measurement conditions (for example, applied voltage and incident power (Supplementary Table 4)). Similar to the trend in Hall effect carrier mobility, the measured responsivity peaks at  $-1.2\%$  strain (Extended Data Fig. 9a). Compressive strain also improves the detectivity and the gain of the photodetector (Extended Data Fig. 9b, c). Devices with a diode structure can reduce the dark current, but have a much lower responsivity: on average 500 times lower than that of the photoconductor-type device (Supplementary Fig. 16).

The strained device also shows an enhanced external quantum efficiency over the visible range (Fig. 5c), owing to the enhanced carrier mobility as well as more efficient carrier transport across the gold-perovskite interface. Additionally, after normalizing the spectra, a distinct response in the short-wave infrared region ( $>810\text{ nm}$ ) can be identified for the strained device (Extended Data Fig. 9d), consistent with the photoluminescence measurements showing bandgap reduction under compressive strain. The rise and fall times of the strained device are around 30% shorter than those of the strain-free device, indicating a faster carrier dynamics (Fig. 5d).

## Online content

Any methods, additional references, Nature Research reporting summaries, source data, extended data, supplementary information, acknowledgements, peer review information; details of author contributions and competing interests; and statements of data and code availability are available at <https://doi.org/10.1038/s41586-019-1868-x>.

- Smith, C. S. Piezoresistance effect in germanium and silicon. *Phys. Rev.* **94**, 42–49 (1954).
- Llordés, A. et al. Nanoscale strain-induced pair suppression as a vortex-pinning mechanism in high-temperature superconductors. *Nat. Mater.* **11**, 329–336 (2012).
- Yang, W. S. et al. Iodide management in formamidinium-lead-halide-based perovskite layers for efficient solar cells. *Science* **356**, 1376–1379 (2017).
- Lin, K. et al. Perovskite light-emitting diodes with external quantum efficiency exceeding 20 per cent. *Nature* **562**, 245–248 (2018).
- Feng, J. et al. Single-crystalline layered metal-halide perovskite nanowires for ultrasensitive photodetectors. *Nat. Electron.* **1**, 404–410 (2018).
- Lü, X. et al. Enhanced structural stability and photo responsiveness of  $\text{CH}_3\text{NH}_3\text{SnI}_3$  perovskite via pressure-induced amorphization and recrystallization. *Adv. Mater.* **28**, 8663–8668 (2016).
- Liu, G. et al. Pressure-induced bandgap optimization in lead-based perovskites with prolonged carrier lifetime and ambient retainability. *Adv. Funct. Mater.* **27**, 1604208 (2017).
- Wang, Y. et al. Pressure-induced phase transformation, reversible amorphization, and anomalous visible light response in organolead bromide perovskite. *J. Am. Chem. Soc.* **137**, 11144–11149 (2015).
- Chen, B. et al. Large electrostrictive response in lead halide perovskites. *Nat. Mater.* **17**, 1164 (2018).
- Zhao, J. et al. Strained hybrid perovskite thin films and their impact on the intrinsic stability of perovskite solar cells. *Sci. Adv.* **3**, eaao5616 (2017).

11. Zhu, C. et al. Strain engineering in perovskite solar cells and its impacts on carrier dynamics. *Nat. Commun.* **10**, 815 (2019).
12. Steele, J. A. et al. Thermal unequilibrium of strained black CsPbI<sub>3</sub> thin films. *Science* **365**, 679–684 (2019).
13. Wang, Y. et al. Nontrivial strength of van der Waals epitaxial interaction in soft perovskites. *Phys. Rev. Mater.* **2**, 076002 (2018).
14. Li, X., et al. Residual nanoscale strain in cesium lead bromide perovskite reduces stability and shifts local luminescence. *Chem. Mater.* **31**, 2778–2785 (2019).
15. Wang, Y. et al. Defect-engineered epitaxial VO<sub>2+δ</sub> in strain engineering of heterogeneous soft crystals. *Sci. Adv.* **4**, eaar3679 (2018).
16. Han, Q. et al. Single crystal formamidinium lead iodide (FAPbI<sub>3</sub>): insight into the structural, optical, and electrical properties. *Adv. Mater.* **28**, 2253–2258 (2016).
17. Fang, Y., Dong, Q., Shao, Y., Yuan, Y. & Huang, J. Highly narrowband perovskite single-crystal photodetectors enabled by surface-charge recombination. *Nat. Photon.* **9**, 679–686 (2015).
18. Pohl, U. W. *Epitaxy of Semiconductors: Introduction to Physical Principles* (Springer, 2013).
19. Chen, T. et al. Entropy-driven structural transition and kinetic trapping in formamidinium lead iodide perovskite. *Sci. Adv.* **2**, e1601650 (2016).
20. Maculan, G. et al. CH<sub>3</sub>NH<sub>3</sub>PbCl<sub>3</sub> single crystals: inverse temperature crystallization and visible-blind UV-photodetector. *J. Phys. Chem. Lett.* **6**, 3781–3786 (2015).
21. Rakita, Y., Cohen, S. R., Kedem, N. K., Hodges, G. & Cahen, D. Mechanical properties of APbX<sub>3</sub> (A=Cs or CH<sub>3</sub>NH<sub>3</sub>; X=I or Br) perovskite single crystals. *MRS Commun.* **5**, 623–629 (2015).
22. Steele, J. A. et al. Direct laser writing of δ- to α-phase transformation in formamidinium lead iodide. *ACS Nano* **11**, 8072–8083 (2017).
23. Li, D. et al. Size-dependent phase transition in methylammonium lead iodide perovskite microplate crystals. *Nat. Commun.* **7**, 11330 (2016).
24. Sarmah, S. P. et al. Double charged surface layers in lead halide perovskite crystals. *Nano Lett.* **17**, 2021–2027 (2017).
25. Kanemitsu, Y. Luminescence spectroscopy of lead-halide perovskites: materials properties and applications to photovoltaic devices. *J. Mater. Chem. C* **5**, 3427–3437 (2017).
26. Xie, L.-Q. et al. Understanding the cubic phase stabilization and crystallization kinetics in mixed cations and halides perovskite single crystals. *J. Am. Chem. Soc.* **139**, 3320–3323 (2017).
27. Katan, C., Mohite, A. D. & Even, J. Entropy in halide perovskites. *Nat. Mater.* **17**, 377–379 (2018).
28. Ge, C. et al. Ultralow thermal conductivity and ultrahigh thermal expansion of single-crystal organic–inorganic hybrid perovskite CH<sub>3</sub>NH<sub>3</sub>PbX<sub>3</sub> (X = Cl, Br, I). *J. Phys. Chem. C* **122**, 15973–15978 (2018).
29. Yin, W.-J., Yang, J.-H., Kang, J., Yan, Y. & Wei, S.-H. Halide perovskite materials for solar cells: a theoretical review. *J. Mater. Chem. A* **3**, 8926–8942 (2015).
30. Giorgi, G., Fujisawa, J.-I., Segawa, H. & Yamashita, K. Small photocarrier effective masses featuring ambipolar transport in methylammonium lead iodide perovskite: a density functional analysis. *J. Phys. Chem. Lett.* **4**, 4213–4216 (2013).
31. Herz, L. M. Charge-carrier mobilities in metal halide perovskites: fundamental mechanisms and limits. *ACS Energy Lett.* **2**, 1539–1548 (2017).
32. Dong, Q. et al. Electron-hole diffusion lengths > 175 μm in solution-grown CH<sub>3</sub>NH<sub>3</sub>PbI<sub>3</sub> single crystals. *Science* **347**, 967–970 (2015).
33. Zheng, X. et al. Improved phase stability of formamidinium lead triiodide perovskite by strain relaxation. *ACS Energy Lett.* **1**, 1014–1020 (2016).
34. Fu, Y. et al. Stabilization of the metastable lead iodide perovskite phase via surface functionalization. *Nano Lett.* **17**, 4405–4414 (2017).
35. Saidaminov, M. I. et al. Suppression of atomic vacancies via incorporation of isovalent small ions to increase the stability of halide perovskite solar cells in ambient air. *Nat. Energy* **3**, 648–654 (2018).
36. Liu, Y. et al. A 1300 mm<sup>2</sup> ultrahigh-performance digital imaging assembly using high-quality perovskite single crystals. *Adv. Mater.* **30**, 1707314 (2018).

**Publisher's note** Springer Nature remains neutral with regard to jurisdictional claims in published maps and institutional affiliations.

© The Author(s), under exclusive licence to Springer Nature Limited 2020

## Methods

### Precursor synthesis

Methylammonium bromine (MABr) was synthesized as the precursor for the substrate growth. First, 20 ml methylamine (40% in methanol, Tokyo Chemical Industry) and 21.2 ml hydrobromic acid (48 wt% in water, Sigma Aldrich) were mixed in an ice bath and the temperature was maintained for the reaction to continue for 2 h. The mixture was heated to 80 °C to evaporate the solvent. The precipitate was dissolved in anhydrous ethanol (Sigma Aldrich) at 80 °C and cooled down for recrystallization. The crystals were then centrifuged with diethyl ether and dried at 80 °C overnight.

### Crystal growth

Methylammonium lead chloride ( $\text{MAPbCl}_3$ ) solution was prepared by mixing 0.675 g of methylammonium chloride (MACl, 98%, Tokyo Chemical Industry) and 2.781 g lead chloride ( $\text{PbCl}_2$ , 99%, Alfa Aesar) in a mixed solution of 5 ml anhydrous dimethylformamide (99.8%, Aldrich) and 5 ml anhydrous dimethyl sulfoxide (DMSO, 99.8%, Aldrich). Methylammonium lead bromine ( $\text{MAPbBr}_3$ ) solution was prepared by mixing 1.120 g MABr and 3.670 g lead bromine ( $\text{PbBr}_2$ , 98%, Acros) in 10 ml dimethylformamide. The  $\text{MAPbCl}_3$  and  $\text{MAPbBr}_3$  solutions were mixed with different ratios. The mixed solutions were kept at room temperature to slowly evaporate the solvent, and single crystals were collected to use as substrates. FAPbI<sub>3</sub> solutions were prepared by mixing formamidinium iodide (FAI, 99.9%, Greatcell Solar) and lead iodide ( $\text{PbI}_2$ , 99.99%, Tokyo Chemical Industry) at a molar ratio of 1:1 in anhydrous gamma-butyrolactone (Sigma Aldrich) with different concentrations. Strain-free  $\alpha$ -FAPbI<sub>3</sub> single crystals were obtained by heating the FAPbI<sub>3</sub> solutions to 120 °C.

### Epitaxial growth

The substrates were heated to different temperatures, and the pre-heated FAPbI<sub>3</sub> solutions (at 100 °C) were then deposited onto the substrates for epitaxial growth.

### Structural and optical characterizations

SEM images were taken with a Zeiss Sigma 500 SEM operated at 3 kV. The  $2\theta/\omega$  XRD patterns, the rocking curve ( $\omega$  scan), and the asymmetrical reciprocal space mapping around the (104) reflection of the substrate were measured by a Rigaku Smartlab diffractometer equipped with a copper  $\text{K}\alpha_1$  radiation source ( $\lambda = 0.15406 \text{ nm}$ ) and a germanium ( $220 \times 2$ ) monochromator. The unit cell parameters ( $a, c$ ) for (104) reflection reciprocal space mapping were converted from ( $Q_x, Q_z$ ) by  $a = 1/Q_x, c = 4/Q_z$ . Raman and photoluminescence spectra were measured by a Raman spectrometer (Renishaw inVia). Raman peak fitting was done by the Renishaw inVia software. Atomic force microscopy was carried out by a scanning probe microscope (Veeco) in a tapping mode. XPS and UPS were carried out by a Kratos AXIS Supra with an aluminium  $\text{K}\alpha$  anode source and a He I (21.22 eV) source, respectively. Measurements were operated under a chamber pressure of  $10^{-8} \text{ torr}$ . XPS data were calibrated with the  $c\text{1s}$  peak (284.8 eV). If not otherwise specified, bulk  $\alpha$ -FAPbI<sub>3</sub> single crystals were used as the strain-free samples for structural and optical characterizations.

### Device fabrication

Devices with a vertical structure were fabricated based on a lithography-based method<sup>37</sup>. Parylene-C (50 nm) and gold (50 nm) were sequentially deposited on the substrates, followed by a photolithography process with photoresist AZ-1512. The pattern was composed of an array of 2-μm-diameter circles (exposed) with 1 μm interdistance (covered by photoresist). The gold was chemically etched with wet etchants and the Parylene-C was precisely etched by reactive ion etching. The etched substrates underwent secondary growth in their corresponding growth solutions so that the substrate surface reached the same height as the electrode. Epitaxial growth on the patterned substrate enabled the  $\alpha$ -FAPbI<sub>3</sub> crystals to initiate from the exposed patterns and gradually merge into a thin film with a controllable

thickness. We note that the  $\text{MAPbCl}_{x}\text{Br}_{3-x}$  substrates were used for the strained devices (heteroepitaxy) and  $\alpha$ -FAPbI<sub>3</sub> substrates were used for the strain-free devices (homoeptaxy). The top electrodes were then deposited by sputtering (for indium tin oxide, 200 nm). For vertical devices, the area of the top electrode was controlled to be  $1 \times 1 \text{ mm}^2$  using a shadow mask. For planar devices, Parylene-C (50 nm) and the electrode (gold, 50 nm) were deposited using a shadow mask with designed electrode layouts.

### Electrical characterizations

Space-charge-limited-current measurements were carried out by a source meter (Keithley 2400) and a customized probe station in a dark environment. Devices with an Au/Perovskite/Au structure were used.  $C-\omega$  measurements were carried out by a parameter analyser (B1500, Agilent) in a dark environment. Devices with an Au/perovskite/indium tin oxide structure were used. The thickness of  $\alpha$ -FAPbI<sub>3</sub> of all devices for space-charge-limited current and  $C-\omega$  measurements was controlled to be 500 nm. Hall effect measurements were carried out with a Lake Shore Hall measurement system (HM 3000) using the van der Pauw method. We note that the Parylene-C layer prevented direct contact between the substrate and electrodes, eliminating possible carriers extracted from the substrate. The thickness of the  $\alpha$ -FAPbI<sub>3</sub> for all devices for Hall effect measurement was controlled to be 500 nm. For the time-of-flight measurement, a 685-nm-pulse laser ( $10 \text{ mW cm}^{-2}$ ) with  $<10^{-10} \text{ s}$  pulse width was used as the light source. Photoresponse was measured with an oscilloscope (MSO6104A Channel Mixed Signal, Agilent). An external bias of 1 V was applied to drive the carriers in the device while a  $1\text{-M}\Omega$  resistor was connected in series to simulate the open-circuit condition so that the carriers were effectively blocked in the devices<sup>32</sup>. The measurement was carried out in the dark while the bias and the laser power were kept constant. The experiment setup followed the reported time-of-flight measurement of halide perovskite single crystals<sup>32,38-40</sup>. The  $\alpha$ -FAPbI<sub>3</sub> thickness of all devices for time-of-flight measurements was also controlled to be 500 nm.

### Photodetector characterizations

Devices with the structure shown in Supplementary Figs. 15 and 16 were used. A 685-nm laser was used as the light source. The  $I-V$  characteristics were collected on a probe station with an Agilent B2912A source meter.

### First-principles calculations

First-principles density functional theory calculations were performed using the Vienna ab initio Simulation Package (VASP)<sup>41</sup>. Electron–ion interactions were described using the Projector Augmented Wave pseudopotential<sup>42</sup>. The electron–electron exchange–correlation functional was treated using the Generalized Gradient Approximation parametrized by Perdew, Burke and Ernzerhof<sup>43</sup>. For bandgap calculations, spin–orbit coupling was incorporated owing to the heavy element Pb, and the hybrid functionals within Heyd–Scuseria–Ernzerhof formalism with 25% Hartree–Fock exchange were employed. A cutoff energy of 400 eV for the plane-wave basis set was used. All structures were fully optimized until all components of the residual forces were smaller than  $0.01 \text{ eV \AA}^{-1}$ . The convergence threshold for self-consistent-field iteration was set at  $10^{-5} \text{ eV}$ . For optimization of the cubic lattice parameter, a  $\Gamma$ -centred  $3 \times 3 \times 3$   $k$ -point mesh was used. A denser  $k$ -point mesh of  $4 \times 4 \times 4$  was used to obtain accurate energies and electronic structures for strained cells. For optimization and static calculations of the heterostructural models,  $\Gamma$ -centred  $4 \times 4 \times 1$  and  $5 \times 5 \times 1$   $k$ -point meshes were used, respectively. Raman intensities were calculated by the CASTEP module in Materials Studios<sup>44</sup> with a  $3 \times 3 \times 3$   $k$ -point mesh and a 400 eV cutoff energy.

### Finite element analysis simulations

Simulation of the current density was done by the multiphysics analysis in COMSOL (version 5.4; www.comsol.com). Simulation of the elastic strain relaxation was done by the ABAQUS<sup>45</sup>.

## Data availability

The data that support the findings of this study are available from the corresponding authors on reasonable request.

37. Lei, Y. et al. Controlled homoepitaxial growth of hybrid perovskites. *Adv. Mater.* **30**, 1705992 (2018).
38. Shi, D. et al. Low trap-state density and long carrier diffusion in organolead trihalide perovskite single crystals. *Science* **347**, 519–522 (2015).
39. Pospisil, J. et al. Density of bulk trap states of hybrid lead halide perovskite single crystals: temperature modulated space-charge-limited-currents. *Sci. Rep.* **9**, 3332 (2019).
40. Saidaminov, M. I. et al. High-quality bulk hybrid perovskite single crystals within minutes by inverse temperature crystallization. *Nat. Commun.* **6**, 7586 (2015).
41. Kresse, G. & Furthmüller, J. Efficient iterative schemes for ab initio total-energy calculations using a plane-wave basis set. *Phys. Rev. B* **54**, 11169–11186 (1996).
42. Blöchl, P. E. Projector augmented-wave method. *Phys. Rev. B* **50**, 17953–17979 (1994).
43. Perdew, J. P., Burke, K. & Ernzerhof, M. Generalized gradient approximation made simple. *Phys. Rev. Lett.* **77**, 3865–3868 (1996).
44. Clark, S. et al. First principles methods using CASTEP. *Z. Kristallogr.* **220**, 567–570 (2005).
45. Smith, M. *ABAQUS/Standard User's Manual Version 6.9* (Dassault Systèmes Simulia Corp, 2009).

**Acknowledgements** We thank T. N. Ng and Z. Wu for guidance on the transient photocurrent measurement; P. Liu and S. Yu for sharing the Rikagu Smartlab diffractometer; D. P. Fenning and X. Li for discussions; Q. Lin for guidance on the reciprocal space mapping measurements; S. Wang for analysis and discussions of the UPS; Y. Zeng for training on the Renishaw inVia

Raman spectrometer; Y. Li, Y. Yin and M. Chen for guidance on the finite element analysis simulations; and S. Xiang for constructive feedback on manuscript preparation. This work was supported by the startup fund by the University of California San Diego. The microfabrication involved in this work was performed at the San Diego Nanotechnology Infrastructure (SDNI) of UCSD, a member of the National Nanotechnology Coordinated Infrastructure, which was supported by the National Science Foundation (grant number ECCS-1542148). KY. acknowledges the National Science Foundation under award number ACI-1550404 and computational resources from Extreme Science and Engineering Discovery Environment (XSEDE), which is supported by National Science Foundation grant number ACI-1548562.

**Author contributions** S.X. and Y.C. conceived the idea. Y.C. and Y. Lei prepared the samples. Y.C. and Y. Lei took the optical and SEM images. Y.C., J.S. and M.-H.C. carried out the XRD, Raman and photoluminescence spectroscopy characterizations. R.R. and A.E.I. contributed to the temperature-dependent photoluminescence characterizations. Y. Li and J.S. carried out the density functional theory calculations. Y.C. and W.C. carried out the finite element analysis simulations. Y.C., Y. Lei, Y.G., C.W. and J.C. contributed to the device fabrication. Y.C., Y.Y. and W.C. carried out the mobility measurements. Y.C. carried out the trap density measurements. Y.C. and Y.Y. carried out the photodetectors characterizations. All authors contributed to analysing the data and commenting on the manuscript.

**Competing interests** The authors declare no competing interests.

### Additional information

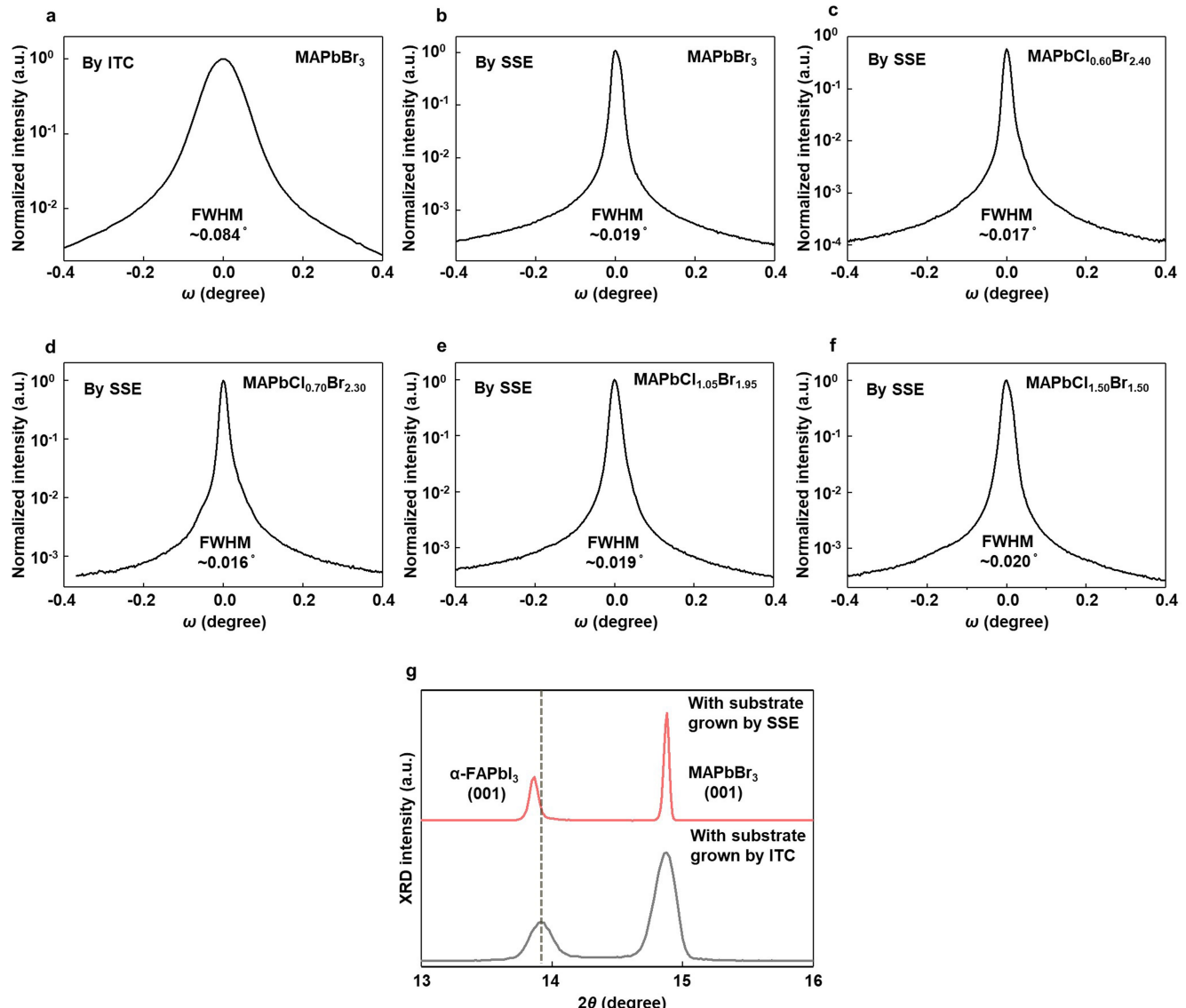
**Supplementary information** is available for this paper at <https://doi.org/10.1038/s41586-019-1868-x>.

**Correspondence and requests for materials** should be addressed to S.X.

**Peer review information** *Nature* thanks Jian Shi, Lijun Zhang and the other, anonymous, reviewer(s) for their contribution to the peer review of this work.

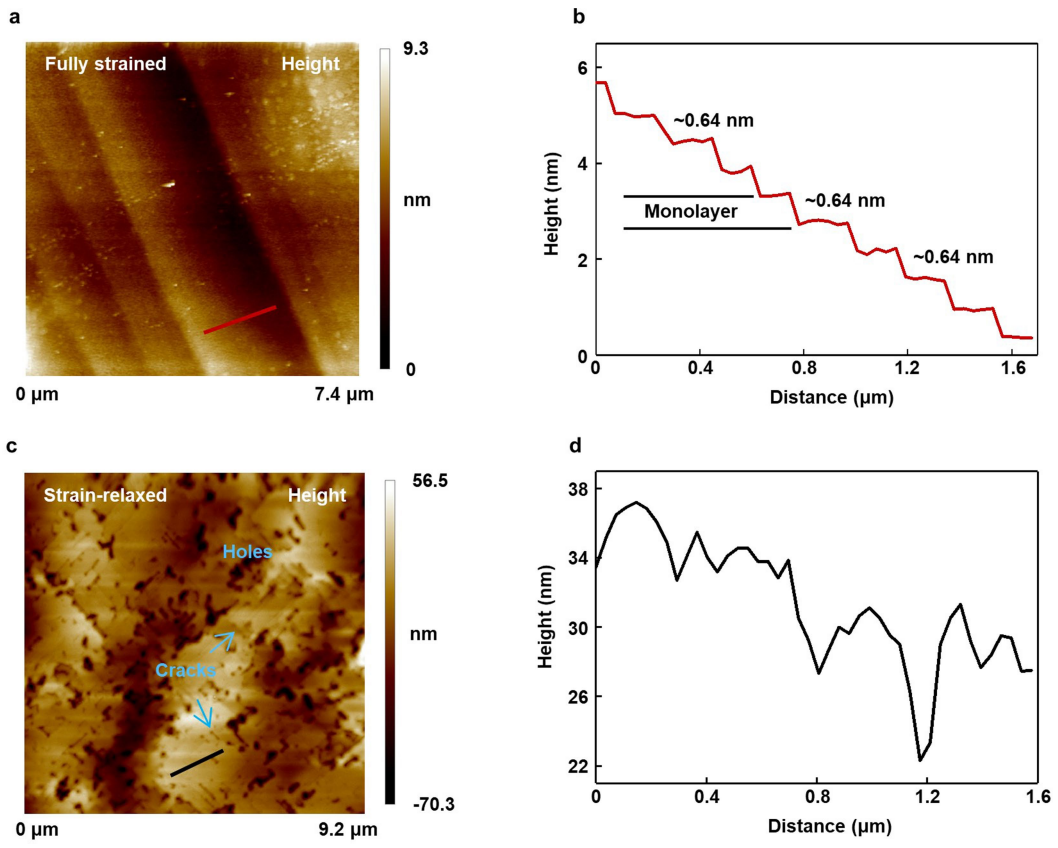
**Reprints and permissions information** is available at <http://www.nature.com/reprints>.

# Article



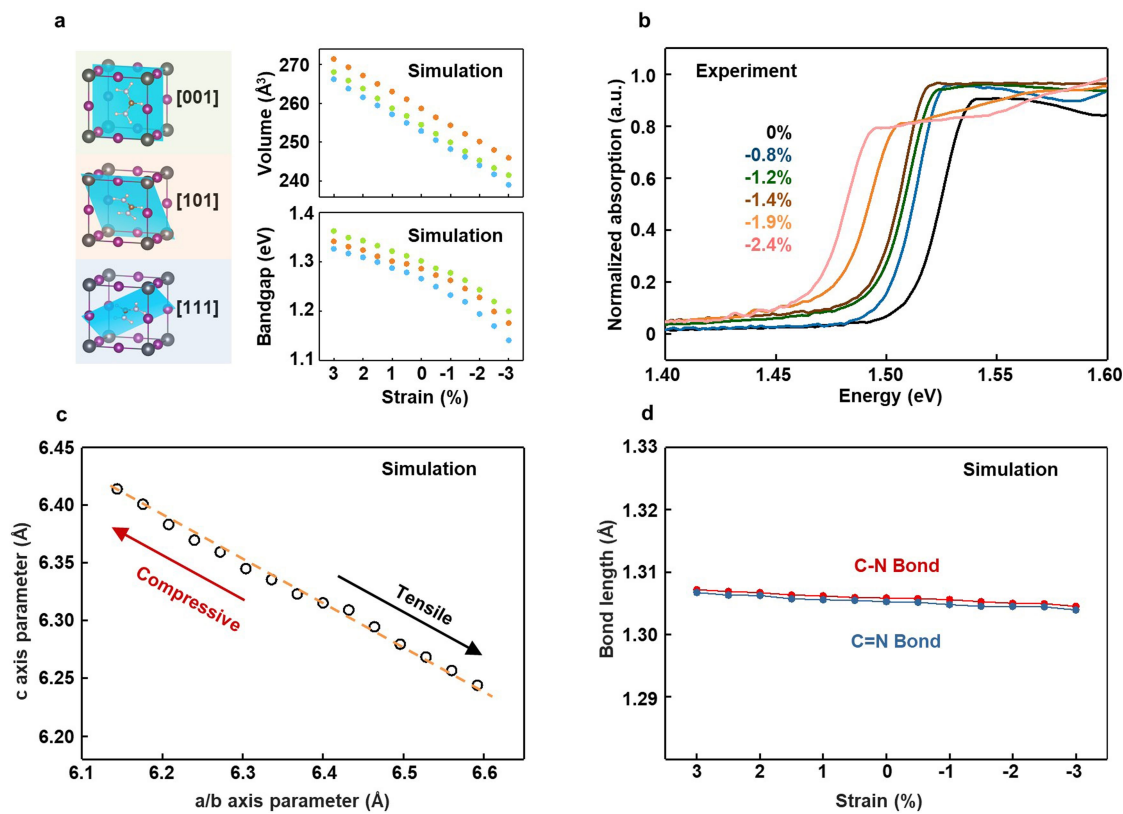
**Extended Data Fig. 1 | Characterization of substrate quality with different growth methods and its impact on the epitaxial strain.** **a–f**, Rocking curve measurements of substrates grown by the inverse temperature crystallization (ITC) and slow solvent evaporation (SSE) methods. Lower full-width at half-maximum (FWHM) values by the SSE indicate better crystal quality. **g**, XRD patterns of strained  $\alpha\text{-FAPbI}_3$  on a substrate with higher crystal quality (red

curve) and relaxed  $\alpha\text{-FAPbI}_3$  on a substrate with lower crystal quality (grey curve). Dislocations in the substrates can propagate into and relax the strain in the epitaxial  $\alpha\text{-FAPbI}_3$ . The vertical dash line labels the (001) peak position of strain-free  $\alpha\text{-FAPbI}_3$ . The peak position from the strain-relaxed  $\text{FAPbI}_3$  (grey curve) shifts back to that of strain-free  $\alpha\text{-FAPbI}_3$ .



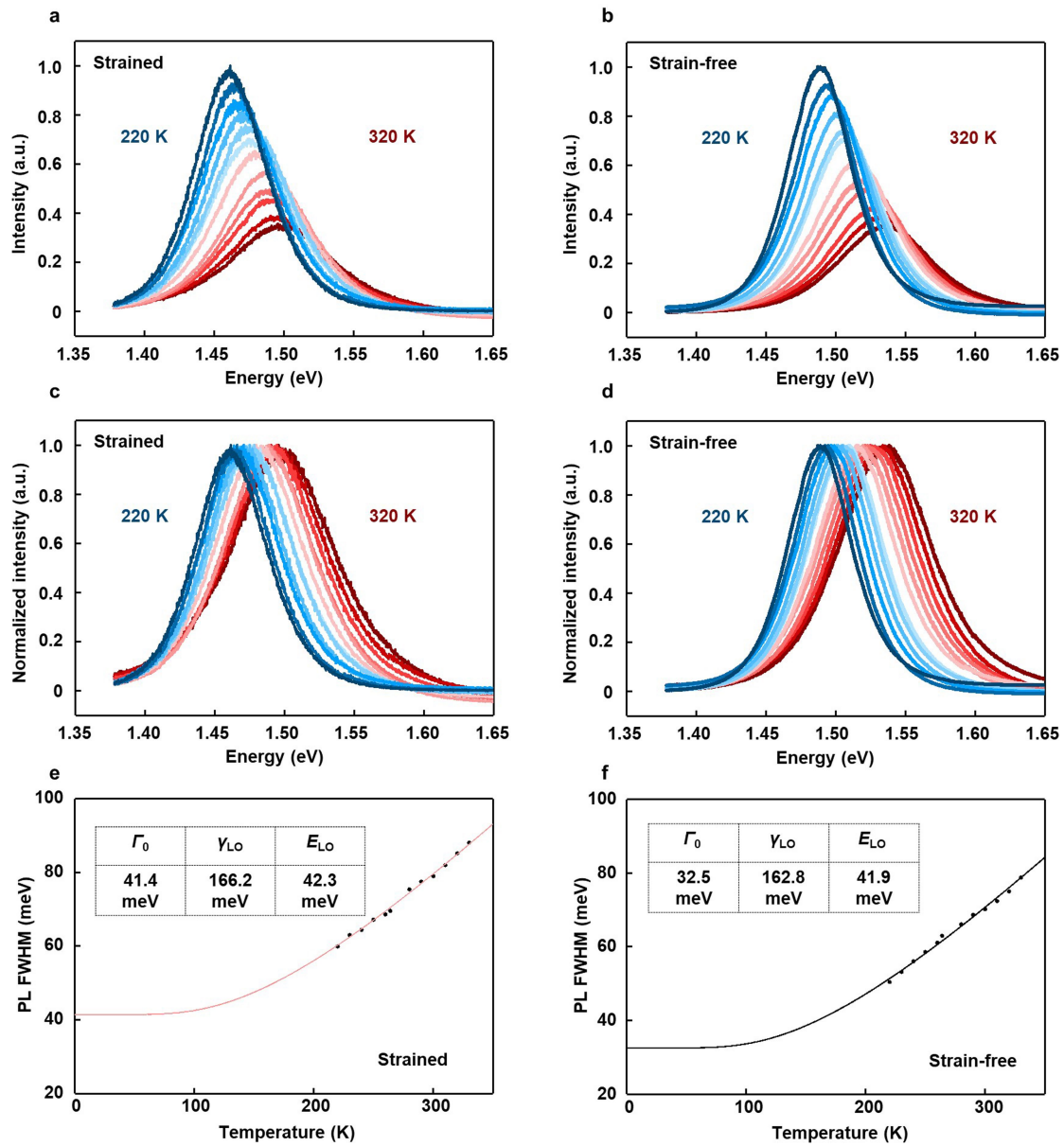
**Extended Data Fig. 2 | Atomic force microscopy morphology characterization of strained and strain-relaxed epitaxial  $\alpha$ -FAPbI<sub>3</sub> films.**  
**a, b.** A topography image (a) and the corresponding height scanning curve (b) of the red line in a of a strained epitaxial  $\alpha$ -FAPbI<sub>3</sub> thin film. **c, d.** A topography image (c) and the corresponding height scanning curve (d) of the black line in c of a strain-relaxed epitaxial  $\alpha$ -FAPbI<sub>3</sub> thick film. Results show that the strained

thin film adopts a layer-by-layer growth model. No cracks or holes can be detected. As the film thickness increases, the total strain energy builds up and generates dislocations that propagate throughout the film and relax the strain, leading to the formation of cracks and holes. These cracks and holes are typically regarded as a signature of strain relaxation.



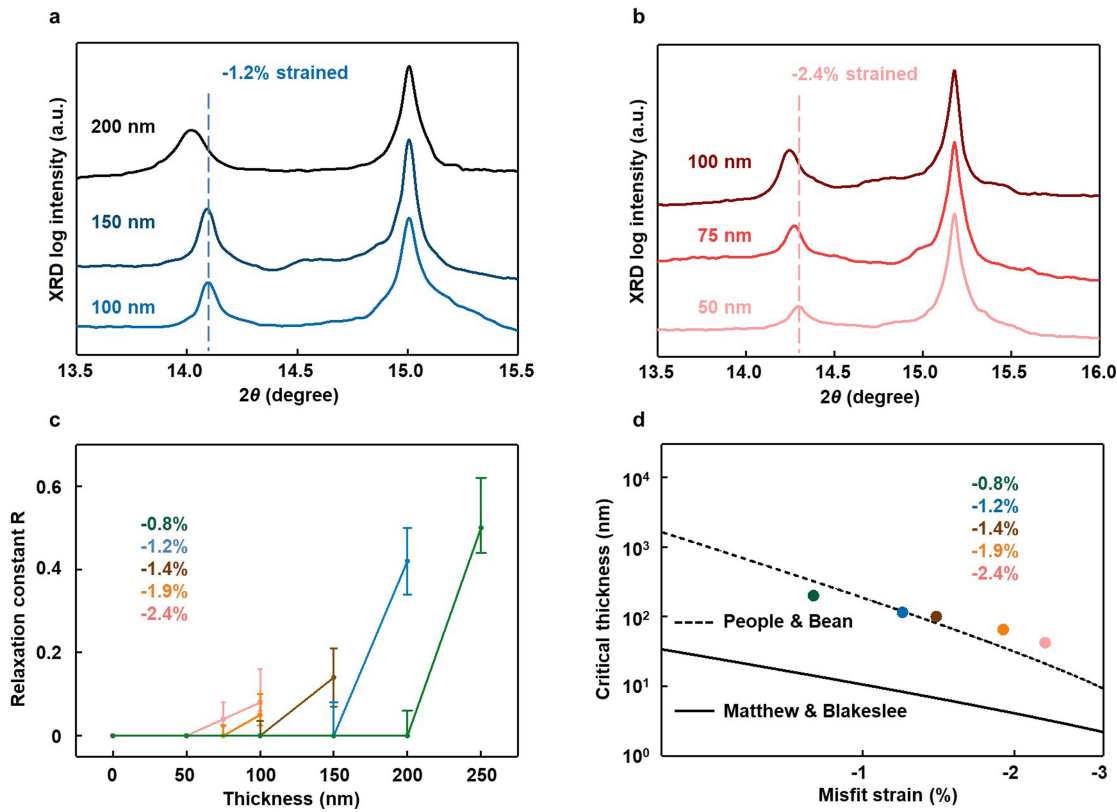
**Extended Data Fig. 3 | First-principles calculations of the strained  $\alpha$ -FAPbI<sub>3</sub> unit cell and experimental absorption spectra of the strained  $\alpha$ -FAPbI<sub>3</sub> under different strains.** **a**, Evolution of lattice volume and bandgap as a function of strain for three  $\alpha$ -FAPbI<sub>3</sub> lattices with different FA<sup>+</sup> organic cation orientations. For the bandgap calculations, spin-orbit coupling is incorporated owing to the heavy element Pb, and the hybrid functionals within Heyd–Scuseria–Ernzerhof formalism with 25% Hartree–Fock exchange are

employed. **b**, The absorption spectra of the strained  $\alpha$ -FAPbI<sub>3</sub> thin films. The absorption onset redshifts with the increasing strain, which agrees with the photoluminescence spectra and prove that the strain can alter the bandgap of the  $\alpha$ -FAPbI<sub>3</sub>. **c**, The c axis length of the unit cell when biaxially straining the *a/b* axes. The slope of the fitted line shows a Poisson's ratio of about 0.3. **d**, C–N and C=N bond lengths at different strain levels. Simulation results show that the deformation of the FA<sup>+</sup> skeleton is very small under the applied biaxial strain.



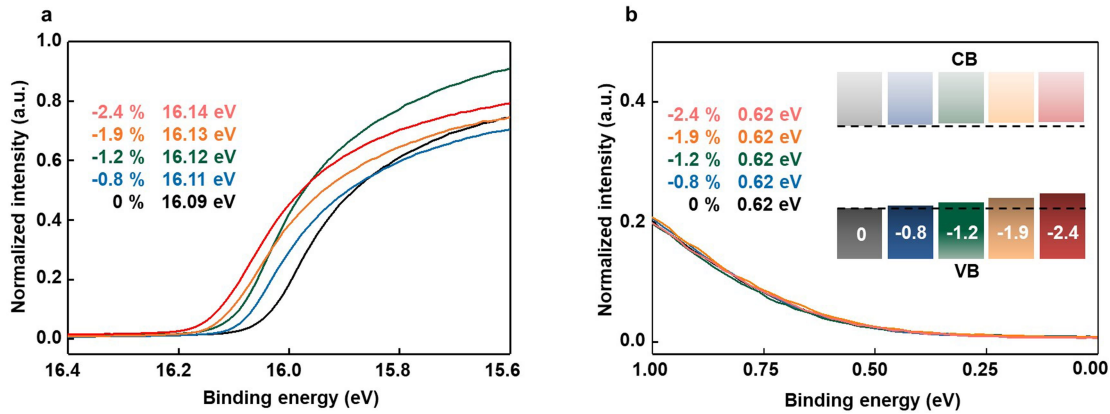
**Extended Data Fig. 4 | Temperature-dependent photoluminescence measurement.** **a, b**, Temperature-dependent photoluminescence of strained (**a**) and strain-free (**b**)  $\alpha$ -FAPbI<sub>3</sub> before normalization. **c, d**, Temperature-dependent photoluminescence of strained (**c**) and strain-free (**d**)  $\alpha$ -FAPbI<sub>3</sub> after normalization. Both samples exhibited uniform bandgap narrowing and FWHM narrowing with decreasing the temperature. **e, f**, Temperature-dependent photoluminescence (PL) FWHM of strained (**e**)  $\alpha$ -FAPbI<sub>3</sub> and strain-

free (**f**)  $\alpha$ -FAPbI<sub>3</sub> with fitting. Results show that the strained  $\alpha$ -FAPbI<sub>3</sub> has a higher  $\Gamma_0$ ,  $\gamma_{\text{LO}}$  and  $E_{\text{LO}}$  than that of strain-free  $\alpha$ -FAPbI<sub>3</sub> owing to the strain-induced crystalline quality reduction and the strain-enhanced carrier-phonon scattering.  $\Gamma_0$ , temperature-independent emission linewidth term associated with the structural disorder scattering.  $\gamma_{\text{LO}}$ , charged-carrier-optical-phonon coupling constant.  $E_{\text{LO}}$ , optical phonon energy.



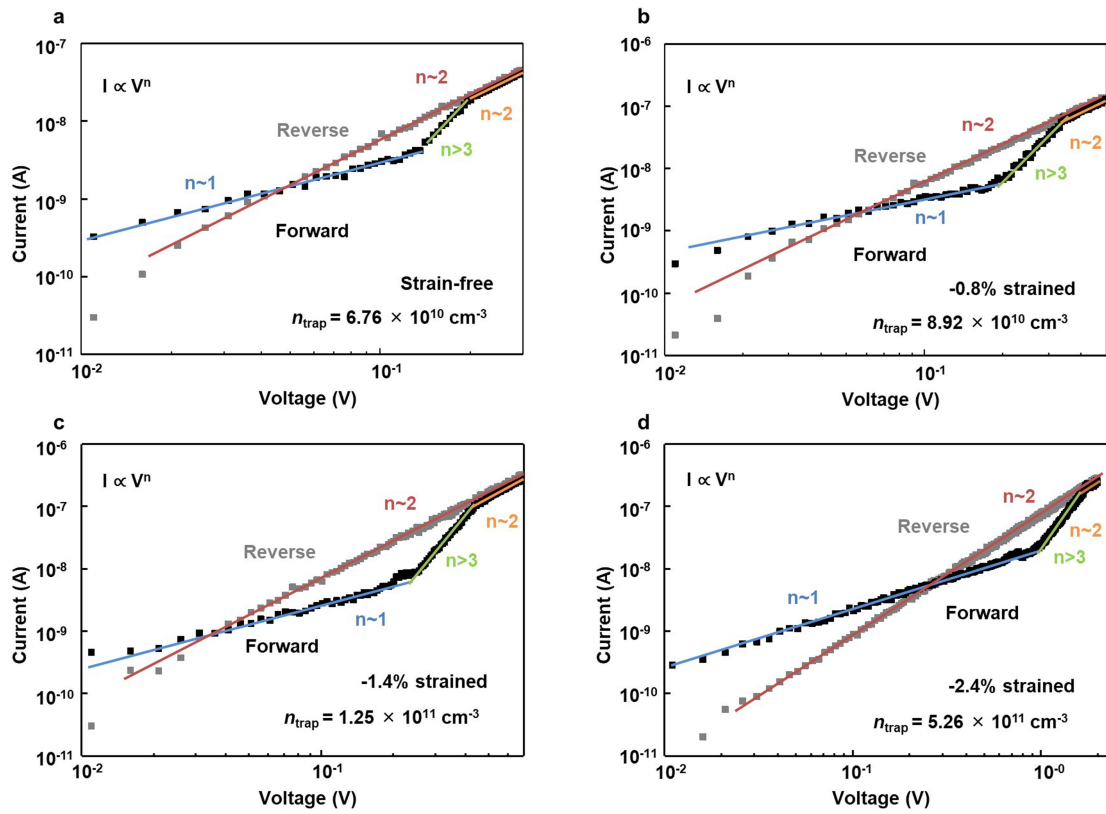
**Extended Data Fig. 5 | Plastic strain relaxation study of the epitaxial  $\alpha$ -FAPbI<sub>3</sub> thin films.** **a, b,** Thickness-dependent in-plane XRD of -1.2% strained (a) and -2.4% strained (b)  $\alpha$ -FAPbI<sub>3</sub> thin films. Vertical lines label the peak position of the fully strained films. Plastic strain relaxation at relatively high thickness can be evident by the peak shifting to lower angle and peak broadening. **c,** Thickness-dependent relaxation constant  $R$  of the epitaxial  $\alpha$ -FAPbI<sub>3</sub> thin films with different strains. Results show that the critical

thickness decreases with increasing strain. **d,** Fitting of the experimental critical thicknesses with the People and Bean and the Matthew and Blakeslee models (see Supplementary Information refs 69 and 70). Experimental results agree well with the People and Bean model, indicating that the plastic strain relaxation due to the dislocations generated during the epitaxial growth is the dominating relaxation mechanism.



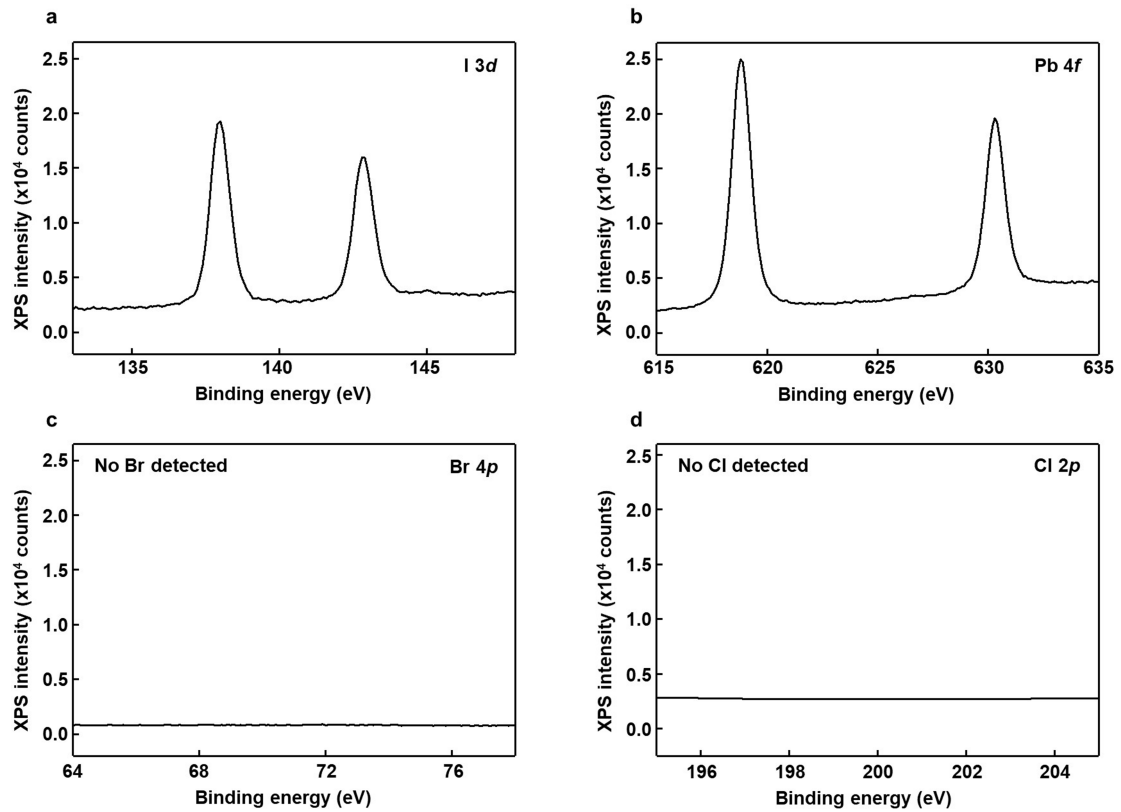
**Extended Data Fig. 6 | UPS spectra of  $\alpha$ -FAPbI<sub>3</sub> under different strains.** **a**, The intersects of the curves with the baseline in the high-binding-energy region give the Fermi level position of corresponding strained  $\alpha$ -FAPbI<sub>3</sub> films. There is a clear shift of the intersects to higher-binding-energy levels when the compressive strain becomes larger. **b**, The intersects of the curves with the

baseline in the low-binding-energy region give the energy difference between the Fermi level and the VBM. All  $\alpha$ -FAPbI<sub>3</sub> films have p-type character according to the calculated Fermi level position in the bandgap. Meanwhile, the VBM is pushed up more than the CBM with increasing strain. Inset, a schematic band diagram of the  $\alpha$ -FAPbI<sub>3</sub> under different strains.

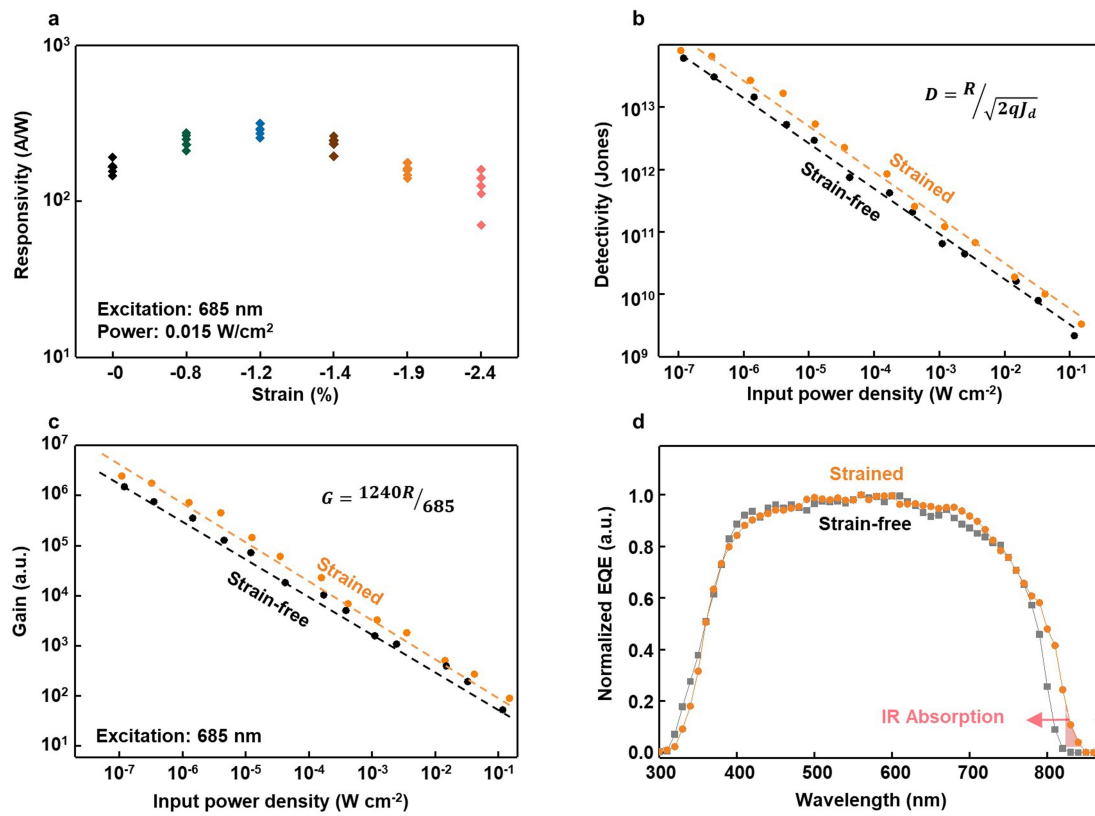


**Extended Data Fig. 7 | Space-charge-limited-current measurement of the epitaxial  $\alpha$ -FAPbI<sub>3</sub> with different strains. a–d,**  $I$ - $V$  characteristic curves for the space-charge-limited-current measurement of the epitaxial  $\alpha$ -FAPbI<sub>3</sub> film with different strains. While the forward scans indicate a typical trap-filling

process with increasing the applied voltage, the reverse scan doesn't show a detrapping process. Number of experiments,  $n = 5$  for each strain value.  $n_{\text{trap}}$ , calculated trap density.



**Extended Data Fig. 8 | XPS spectra of strained  $\alpha$ -FAPbI<sub>3</sub>.** XPS spectra of: **a**, I 3d; **b**, Pb 4f; **c**, Br 4p; and **d**, Cl 2p photoelectrons from a strained  $\alpha$ -FAPbI<sub>3</sub> film. Results show that Br and Cl are absent in the strained  $\alpha$ -FAPbI<sub>3</sub>.



**Extended Data Fig. 9 | Photoconductor-type photodetector characterizations with a 685-nm laser.** **a**, Responsivity as a function of strain level in  $\alpha$ -FAPbI<sub>3</sub>. Devices under  $-0.8\%$ ,  $-1.2\%$  and  $-1.4\%$  compressive strain give better responsivity compared to the strain-free devices. Further increasing the compressive strain can lead to a higher density of dislocations, which reduces the responsivity. Number of experiments,  $n = 5$  for each strain value.

**b, c**, Detectivity (**b**) and gain  $G$  (**c**) of the photodetector based on  $\alpha$ -FAPbI<sub>3</sub> under  $-1.2\%$  strain, indicating enhanced performance.  $q$ , element charge.  $J_d$ , dark current density. **d**, Normalized external quantum efficiency (EQE) of the photodetector based on  $\alpha$ -FAPbI<sub>3</sub> under  $-1.2\%$  strain, showing an extended infrared absorption range.